Cheng, Z., Martial, M.E., Zhang, Z., Li, J., Xu, L., and Krmíček, L., 2023, Heterogeneous mush-dominated plumbing system and mantle sources of alkaline lamprophyres in Tuoyun Basin, SW Central Asian Orogenic Belt: GSA Bulletin, https://doi.org/10.1130/B36951.1.

Supplementary material

Text S1. Analytical Methods

Figure S1: Chemical variations of the clinopyroxene in the Tuoyun lamprophyres

Figure S2: Chemical variations of the amphibole in the Tuoyun lamprophyres

Figure S3: LOI values vs. $(^{87}Sr/^{86}Sr)_t$ and $\varepsilon_{Nd}(t)$ diagrams

Figure S4: Comparison between the Tuoyun monchiquite I, II, monchiquite and camptonite and the experimental melts

Table S1. The sample locality of the Tuoyun monchiquite I, II and camptonite studied in the present study

Table S2. The results of standards used during the analysis of olivine, clinopyroxene and amphibole by EMPA

Table S3. Olivine major elemental compositions (wt.%) analyzed by EMPA in the Tuoyun monchiquite I

Table S4. Clinopyroxene major elemental compositions (wt.%) analyzed by EMPA and P-T estimates in the Tuoyun monchiquite I, II and camptonite

Table S5. Amphibole major elemental compositions (wt.%) analyzed by EMPA and P-T-H_2O estimates in the Tuoyun monchiquite I and camptonite

Table S6. The water contents in the clinopyroxene megacrysts (ppm) and the corresponding melt (wt.%) of the monchiquite I based on FTIR

Table S7. The major (wt.%) and trace elements (ppm) of standards of AGV-2 and GSR-3

Table S8. Major (wt.%) and trace elements (ppm) of the Tuoyun monchiquite I, II and camptonite

Table S9. Sr-Nd isotopic compositions of the Tuoyun monchiquite I, II and camptonite

Table S10. Olivine SIMS in situ oxygen isotopic compositions (‰) of the monchiquite I

SUPPLEMENTAL TEXT S1

Analytical Methods

Electron Microprobe Analyses (EMPA)

Mineral major compositions were determined at the EMPA Lab using an EPMA1720 electron microprobe, China University of Geosciences, Beijing. The analyses were conducted in a wavelength dispersive mode. The condition is condition is 15 kV acceleration voltage, 10 nA beam current and 1-2μm focused beam width. The peak counting time is 50s for Ca, 30s for Ni, 20s for Mg, Fe and 10s for the other elements, while the background duration is 10 s, respectively. Natural minerals (Mineral Standard Mount NINM25-53, Astimex Scientific) and synthetic oxides were used for calibration of different elements. The data were corrected by the ZAF3 on-line analytical procedure. Relative errors are <1% for major elements and <10% for minor elements. The results of standards are presented in Table S2, and the results of olivine, clinopyroxene and amphibole are listed in Tables S3-S5.

Fourier Transform Infrared Spectroscopy (FTIR)

Clinopyroxene megacrysts were selected to determine the H_2O concentrations by FTIR installed at the State Key Laboratory for Mineral Deposits Research, Nanjing University. The samples were firstly double-side polished and pasted on a glass slide for petrographic observation. Secondly, the clinopyroxene megacrysts with no optically visible inclusions or cracks were selected for FTIR analysis. The apertures are 40×40 μm, and the focused spots are located at the same grains of EMPA. The FTIR spectra were performed at room temperature by a BRUKER VERTEX 70V spectrometer equipped with a HYPERION 2000 infrared microscope. The analyzed resolution of the spectrometer is better than 4 cm^{-1}. Unpolarized absorption measurement was adopted, and the spectral ranges from 650 to 4500 cm^{-1}. A total of 128 scans were counted for each spectrum. Water contents in the clinopyroxene were calculated based on the Beer-Lambert law: $c=A/(\varepsilon \cdot l)$. Therein, c is the concentration of hydrogen species (ppm H_2O), A is the integral absorption area (cm^{-1}), ε is the absorption coefficient (0.704 $ppm^{-1} \cdot cm^{-2}$ for clinopyroxene; Bell et al., 1995) and l is the thickness of the plate (70 μm in this study). The integral region was 3000-3800 cm^{-1}.

Bulk-rock Major and Trace Elements

Both xenoliths and megacrysts were carefully removed before they were crushed to powder. Bulk-rock major and trace elements were measured at the State Key Laboratory of Geological Processes and Mineral Resources, China University of Geosciences, Beijing. About 50 mg powder was weighted and totally dissolved in alkali solution, and then diluent to a constant volume in purified HNO_3 prepared for measurement. Major element analysis was performed by LEEMAN LABS.INC Prodigy inductively coupled plasma Optical Emission Spectrometry (ICP-OES). The loss on ignition (LOI) was measured by the mass loss of 100mg rock powder before and after heating at 980℃ for 60 min in the Muffle furnace. Two standards of AGV-2 from U.S. Geological Survey (USGS) and GSR-3 from National Research Centre for Geoanalysis were adopted to monitor the uncertainties that are less than 1%. In addition, ~40 mg powder was weighted for trace elemental measurement and they were dissolved in the autoclave with HNO_3-HF solution. The trace elements were measured by Agilent 7500a LA-ICP-MS. During the measurement, AGV2 and GSR-3 were used to monitor the uncertainties. Cr, Sc, Cu, Zn, Sr, and Ta are better than 10% and the other elements are less than 5%. The results of standards of AGV-2 and GSR-3 are listed in Table S6.

Bulk-rock Sr-Nd Isotopes

Sr-Nd isotopic compositions were measured by the *Neptune Plus* multi-collector inductively coupled mass spectrometry (MC-ICP-MS) at the State Key Laboratory of Geological Processes and Mineral Resources, China University of Geosciences, Beijing. The powder of rock was firstly dissolved in the PFA beakers (Savillex®) within the HF-HNO_3-HCl solution. Sr and Nd were then purified by the cation exchange columns in the pre-cleaned Bio-Rad cation AG50W-X12 resin and LN resin with HCl, respectively. The long-term reference value was $^{87}Sr/^{86}Sr$=0.710257±11 (2σ, n=32) for NIST SRM 987 and $^{143}Nd/^{144}Nd$=0.512428±8 (2σ, n=32) for Alfa Nd, which are used as an in-house reference standard. The employed standard BHVO-2 yielded $^{87}Sr/^{86}Sr$ of 0.703561±12 and $^{143}Nd/^{144}Nd$ of 0.512977±7. The results are consistent with the recommended values within uncertainties (Xu et al., 2021). Mass fractionations were calibrated by $^{86}Sr/^{88}Sr$ = 0.1194 and $^{146}Nd/^{144}Nd$ = 0.7219 based on the exponential law.

Olivine SIMS Oxygen Isotope Analysis

Olivine *in situ* oxygen isotopes were carried out by Cameca IMS 1280 at Institute of Geology and Geophysics, Chinese Academy of Sciences. Secondary ions were performed in the

multi-collection mode under the condition of an acceleration voltage of 10 kV, Cs^+ primary ion beam of ca. 2 nA and 10 μm diameter. During the running, Au-coated samples were fired 25×25 μm area for 150 s, and then drilled 10×10 μm area at central. Secondary ions were run for 200 s, and it totally took ~4 min for each spot. The instrumental mass fractionation factor (IMF) was corrected using the olivine standard San Carlos. Measured $^{18}O/^{16}O$ values are normalized to Vienna standard mean ocean water (V_{SMOW}; Baertschi, 1976). The internal precision was better than 0.2 ‰ for $^{18}O/^{16}O$. Detailed analytical procedures have been described by Li et al. (2010) and Tang et al. (2015, 2019).

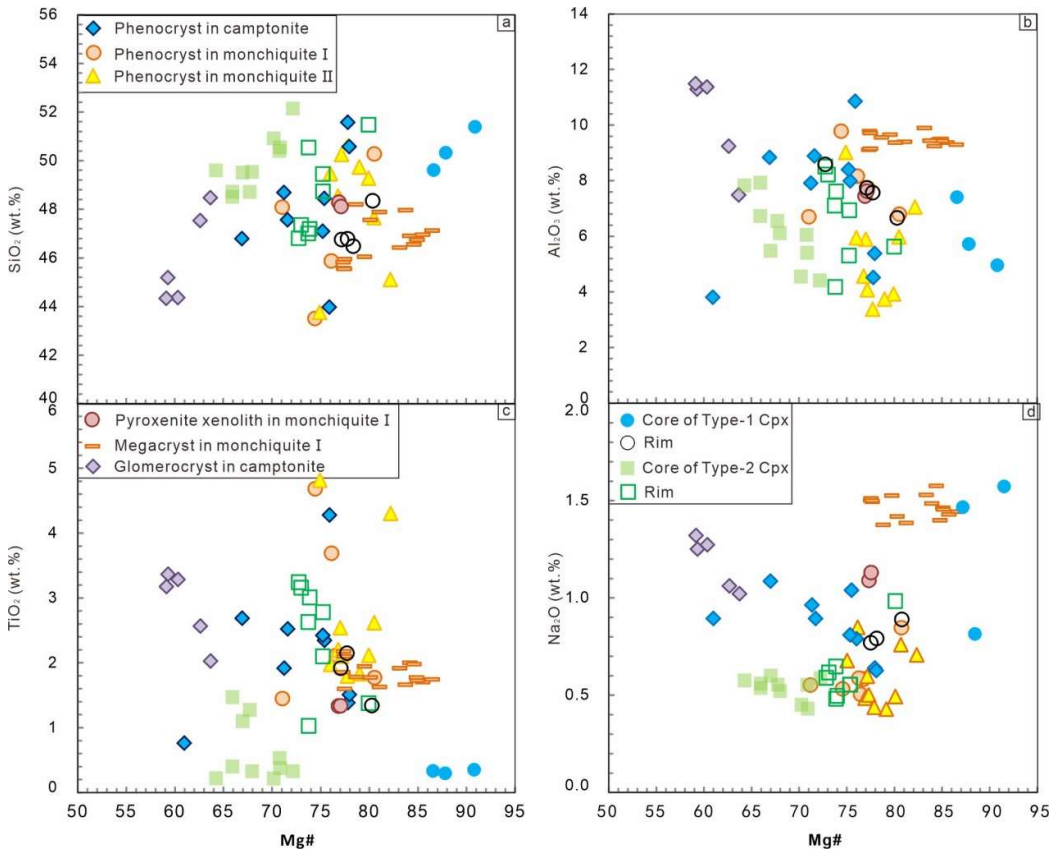

Figure S1. Chemical variations of the (zoned) clinopyroxene phenocrysts, xenocrysts, megacrysts, pyroxenite xenoliths, glomeracrysts, zoned clinopyroxene in the monchiquite I, II and camptonite.

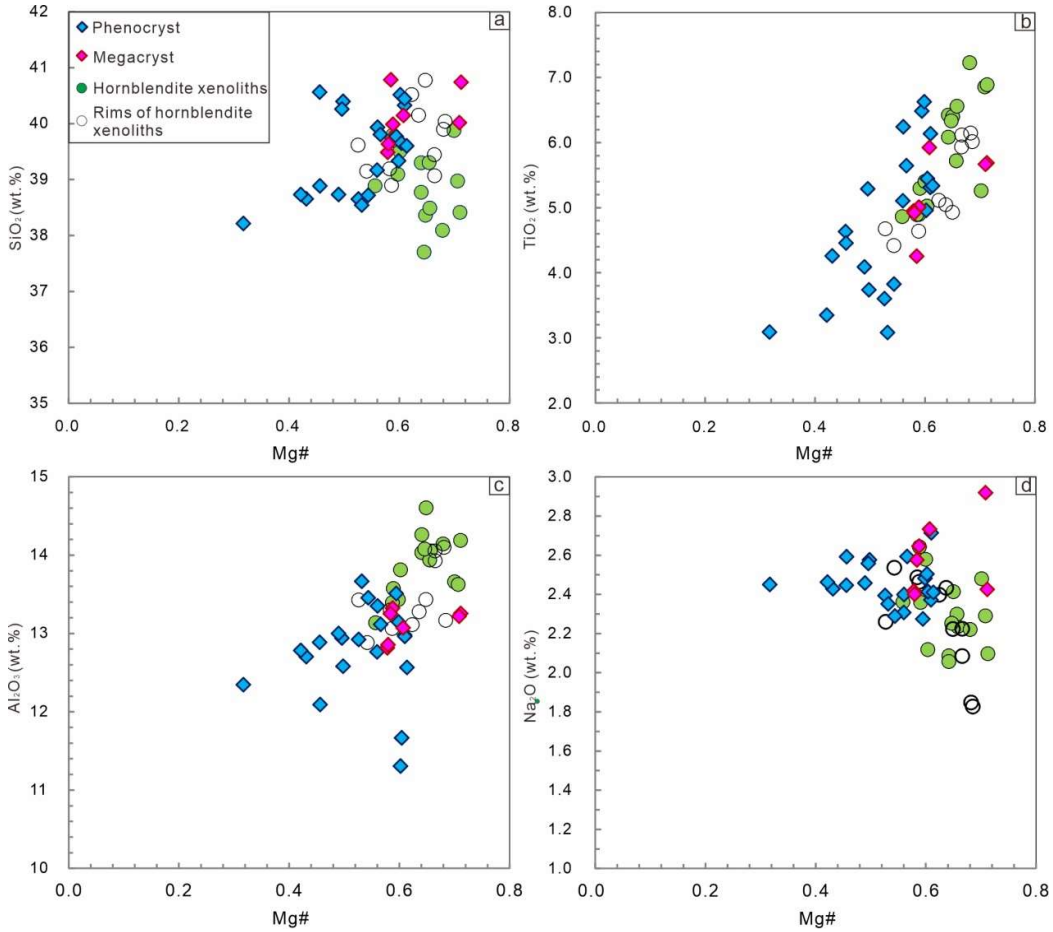

Figure S2. Chemical variations of the amphibole phenocrysts, megacrysts, hornblendite xenoliths and the reacted rims.

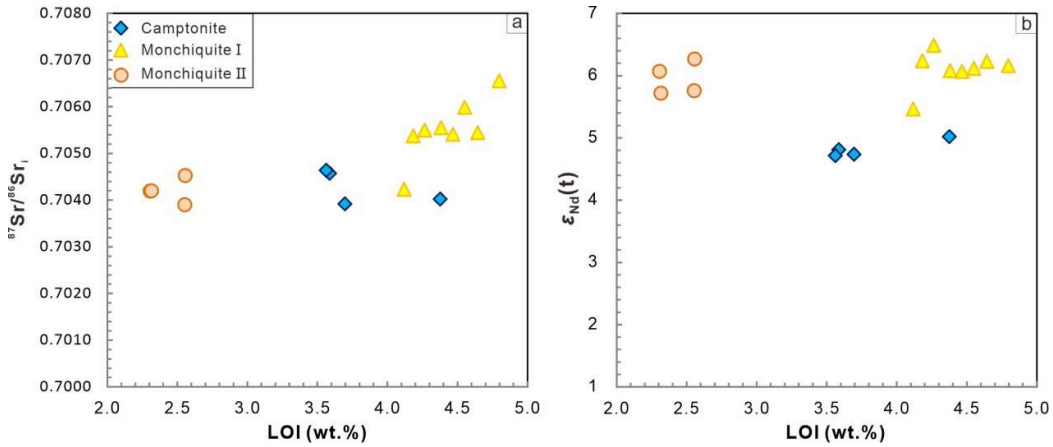

Figure S3. (a) LOI values vs. $(^{87}Sr/^{86}Sr)_t$ diagrams showing the influence of secondary alteration on the Sr isotopes. (b) LOI values vs. $\varepsilon_{Nd}(t)$ diagrams showing the influence of secondary alteration on the Nd isotopes.

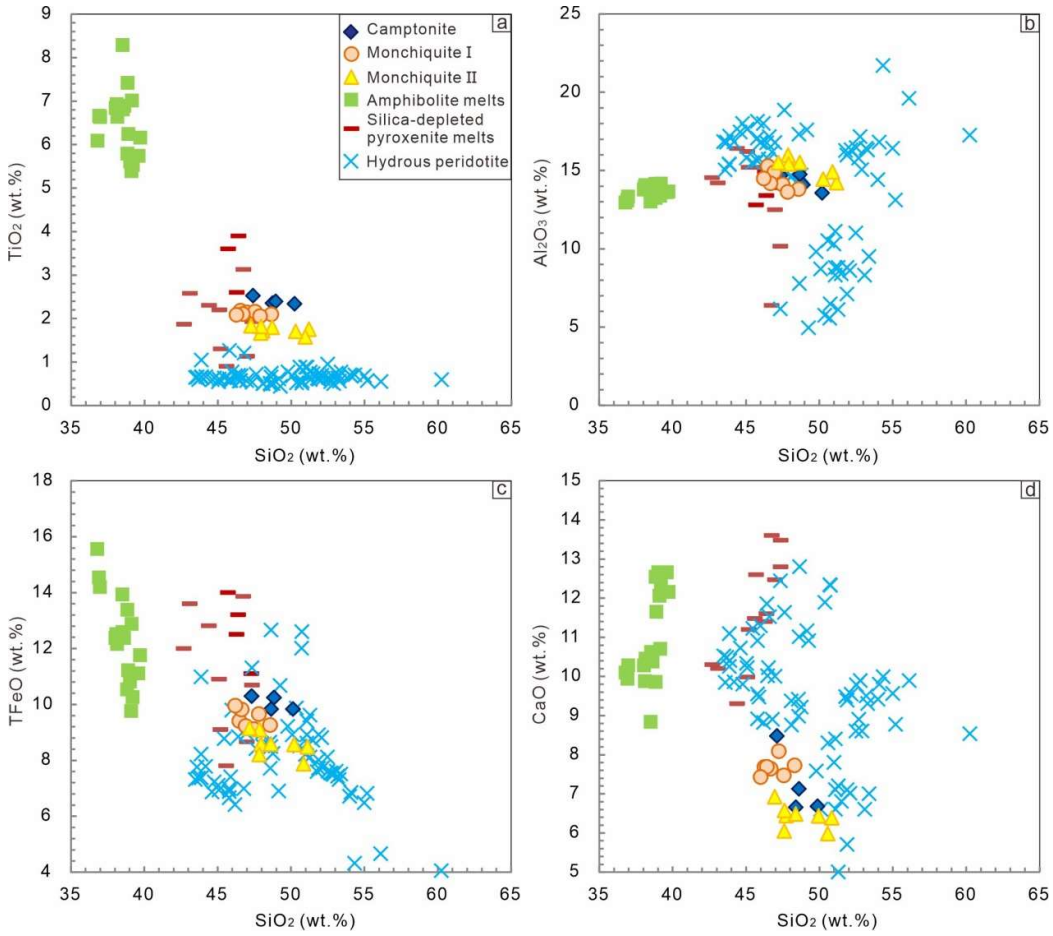

Figure S4. Comparison between the Tuoyun monchiquite I, II, monchiquite and camptonite and the experimental melts. Data source: Partial melts of amphibolite from Pilet et al. (2008), Silica-depleted pyroxenite from Hirschmann et al. (2003) and Kogiso et al. (2003), Hydrous peridotite from Hirose (1997), Gaetani and Grove (1998), Falloon and Danyushevsky (2000), Laporte et al. (2004), Parman and Grove (2004), Baker et al. (1994) and Wood & Turner (2009).

REFERENCES CITED

Baertschi, P., 1976, Absolute ^{18}O content of standard mean ocean water: Earth and Planetary Science Letters, v. 31, p. 341-344, https://doi.org/10.1016/0012-821X(76)90115-1.

Baker, M., Grove, T., and Price, R., 1994, Primitive basalts and andesites from the Mt. Shasta region, N. California: products of varying melt fraction and water content: Contributions to Mineralogy and Petrology, v. 118, p. 111-129,

https://doi.org/10.1007/BF01052863.

Bell, D.R., Ihinger, P.D., and Rossman, G.R., 1995, Quantitative analysis of trace OH in garnet and pyroxenes: American Mineralogist, v. 80, p. 465-474, https://doi.org/10.2138/am-1995-5-608.

Falloon, T.J., and Danyushevshy, L.V., 2000, Melting of refractory Mantle at 1.5, 2 and 2.5 GPa under anhydrous and H_2O-undersaturated conditions: Implications for the petrogenesis of high-Ca boninites and the influence of subduction components on mantle melting: Journal of Petrology, v. 41, p. 257-283, https://doi.org/10.1093/petrology/41.2.257.

Gaetani, G.A., and Grove, T.L., 1998, The influence of water on melting of mantle peridotite: Contributions to Mineralogy and Petrology, v. 131, p. 323-346, https://doi.org/10.1007/s004100050396.

Hirose, K., 1997, Melting experiments on lherzolite KLB-1 under hydrous conditions and generation of high-magnesian andesitic melts: Geology, v. 25, p. 42-44, https://doi.org/10.1130/0091-7613(1997)0252.3.CO;2.

Hirschmann, M.M., Kogiso, T., Baker, M.B., and Stolper, E.M., 2003, Alkalic magmas generated by partial melting of garnet pyroxenite: Geology, v. 31, p. 481-484, https://doi.org/10.1130/0091-7613(2003)0312.0.CO;2.

Kogiso, T., Hirschmann, M.M., and Frost, D.J., 2003, High-pressure partial melting of garnet pyroxenite: possible mafic lithologies in the source of ocean island basalts: Earth and Planetary Science Letters, v. 216, p. 603-617, https://doi.org/10.1016/S0012-821X(03)00538-7

Laporte, D., Toplis, M., Seyler, M., and Devidal, J., 2004, A new experimental technique for extracting liquids from peridotite at very low degrees of melting: application to partial melting of depleted peridotite: Contributions to Mineralogy and Petrology, v. 146, p. 463-484.

Li, X.H., Li, W.X., Li, Q.L., Wang, X.C., Liu, Y., and Yang, Y.H., 2010, Petrogenesis and tectonic significance of the ~850 Ma Gangbian alkaline complex in South China: Evidence from in situ zircon U-Pb dating, Hf-O isotopes and whole-rock geochemistry: Lithos, v. 114, p. 1-15. https://doi.org/10.1016/j.lithos.2009.07.011

Parman, S.W., and Grove, T.L., 2004, Harzburgite melting with and without H2O: Experimental data and predictive modeling: Journal of Geophysical Research-Solid Earth, v. 109, B02201, https://doi.org/10.1029/2003JB002566.

Pilet, S., Baker, M.B., and Stolper, E.M., 2008, Metasomatized lithosphere and the origin of alkaline Lavas: Science, v. 320, p. 916-919, https://doi.org/10.1126/science.1156563.

Tang, G.Q., Li, X.H., Li, Q.L., Liu, Y., Ling, X.X., and Yin, Q.Z., 2015, Deciphering the physical mechanism of the topography effect for oxygen isotope measurements using a Cameca IMS-1280 SIMS: Journal of Analytical Atomic Spectrometry, 30(4), 950-956, https://doi.org/10.1039/C4JA00458B.

Tang, G.Q., Su, B.X., Li, Q.L., Xia, X.P., Jing, J.J., Feng, L.J., Martin, L., Yang, Q., and Li, X.H., 2019, High-Mg# Olivine, Clinopyroxene and Orthopyroxene Reference Materials for In Situ Oxygen Isotope Determination: Geostandards And Geoanalytical Research, v. 43, p. 585-593, https://doi.org/10.1111/ggr.12288.

Wood, B.J., and Turner, S.P., 2009, Origin of primitive high-Mg andesite: Constraints from natural examples and experiments: Earth and Planetary Science Letters, v. 283, p. 59-66, https://doi.org/10.1016/j.epsl.2009.03.032.

Xu, L.J., Liu, S.A., and Li, S.G., 2021, Zinc isotopic behavior of mafic rocks during continental deep subduction: Geoscience Frontiers, v. 12, 101182, https://doi.org/10.1016/j.gsf.2021.101182.